High-precision tumor resection down to few-cell level guided by NIR-IIb molecular fluorescence imaging

Feifei Wang[a,b,1], Liangqiong Qu[c,1], Fuqiang Ren[a,b,1], Ani Baghdasaryan[a,b,1], Yingying Jiang[a,b,1], RuSiou Hsu[a,b,1], Peng Liang[a,b], Jiachen Li[a,b], Guanzhou Zhu[a,b], Zhuoran Ma[a,b], and Hongjie Dai[a,b,2]

In vivo fluorescence/luminescence imaging in the near-infrared-IIb (NIR-IIb, 1,500 to 1,700 nm) window under <1,000 nm excitation can afford subcentimeter imaging depth without any tissue autofluorescence, promising high-precision intraoperative navigation in the clinic. Here, we developed a compact imager for concurrent visible photographic and NIR-II (1,000 to 3,000 nm) fluorescence imaging for preclinical image-guided surgery. Biocompatible erbium-based rare-earth nanoparticles (ErNPs) with bright down-conversion luminescence in the NIR-IIb window were conjugated to TRC105 antibody for molecular imaging of CD105 angiogenesis markers in 4T1 murine breast tumors. Under a ~940 ± 38 nm light-emitting diode (LED) excitation, NIR-IIb imaging of 1,500- to 1,700-nm emission afforded noninvasive tumor–to–normal tissue (T/NT) signal ratios of ~40 before surgery and an ultrahigh intraoperative tumor-to-muscle (T/M) ratio of ~300, resolving tumor margin unambiguously without interfering background signal from surrounding healthy tissues. High-resolution imaging resolved small numbers of residual cancer cells during surgery, allowing thorough and nonexcessive tumor removal at the few-cell level. NIR-IIb molecular imaging afforded 10-times-higher and 100-times-higher T/NT and T/M ratios, respectively, than imaging with IRDye800CW-TRC105 in the ~900- to 1,300-nm range. The vastly improved resolution of tumor margin and diminished background open a paradigm of molecular imaging-guided surgery.

short-wave infrared | fluorescence imaging | image-guided surgery | molecular imaging | NIR-IIb imaging

Surgical removal of tumor has been performed to combat cancer in conjunction with chemotherapy, radiation therapy, hormone therapy, and immunotherapy. For over a century, surgeons have relied on visual feedback and experience to identify margins between malignant and healthy tissues, with the caveats of leaving cancerous residues or removing heathy tissues excessively (1). Tumor residues appeared in 8 to 70% of cases of radical prostatectomies, pancreaticoduodenectomies, breast cancer, and high-grade glioma excision (2–4), leading to local cancer recurrence. MRI, CT, or X-rays are used to improve preoperative imaging (early detection, surgical planning, etc.) but are not applicable to real-time intraoperative navigation (2). Ultrasonography can be used to guide surgery, but surgical manipulation causes artifacts and decreases the image quality (5). Further, thus far, no imaging modality exists for spatially resolving and removing tumor at the few-cell level.

Near-infrared (NIR) fluorescence imaging has been used for preclinical and clinical intraoperative navigation with real-time and high-spatial-resolution capabilities. The US Food and Drug Administration (FDA) approved the NIR-I (700 to 1,000 nm) fluorophore indocyanine green (ICG) for clinical use, and a similar dye, IRDye800CW, was used in human clinical trials for tumor or sentinel lymph nodes localization (6, 7), metastasectomy (8), and coronary angiography (9). Molecular fluorescence imaging using targeted contrast agents (2) such as IRDye800CW bio-conjugated to bevacizumab has been used to image human tumors overexpressing vascular endothelial growth factor (10). NIR-I imaging in the 800- to 900-nm window with such probes afforded tumor–to–normal tissue (T/NT) ratio of 1.1 to 7.0 (8, 10–13), limited by high background signals due to nonspecific binding or uptake of the probes by normal tissues (12), light scattering, and autofluorescence (14). Much higher T/NT ratios are desired in order to prevent ambiguity in tumor margin and enable more precise tumor resection. Such capability could revolutionize oncological surgery (3).

Since 2009, fluorescence imaging in the NIR-II window (1,000 to 3,000 nm) (15, 16) has been explored for preclinical and clinical imaging to afford deeper penetration depth, lower background, and higher resolution than NIR-I imaging, taking advantage of reduced light scattering and diminished tissue autofluorescence at long wavelengths

(11, 15, 17–26). Various probes with emission in the NIR-II window have been developed, including small organic molecules (17, 18), carbon nanotubes (15, 27, 28), quantum dots (16, 19, 20), and rare-earth down-conversion nanoparticles (21–23). These probes led to in vivo one-photon wide-field (14, 15, 20, 27–30), confocal (16, 19), light sheet (24), and structured illumination (25) fluorescence imaging at subcentimeter depths in whole-body or microscopy modes with down to single-cell resolution, facilitating investigations of mouse models of cardiovascular and brain diseases and cancer models including immunotherapy (20, 21, 28, 31, 32).

NIR-II imaging-guided tumor resection is promising to improve T/NT and tumor margin determination, allowing more precise tumor resection. Thus far, preclinical imaging in the 1,000- to 1,300-nm range has demonstrated T/NT ratios of 4 to 15 before surgery and intraoperative tumor-to-muscle (T/M) or peripheral tissue signal ratios of 4 to 13 by using organic fluorophores (26, 30, 31, 33, 34) or Nd-based down-conversion nanoparticles conjugated to targeting ligands (35, 36). Conventional NIR-I ICG and IRDye800CW dyes exhibited fluorescence emission tails in the short-wavelength region of the NIR-II window (1,000 to 1,300 nm) (37) and were utilized for intraoperative NIR-II imaging in preclinical and clinical trials (1, 2, 6, 10, 11). It was shown that the T/NT ratios in the 1,000- to 1,300-nm window were ~2 times of those in the NIR-I window with ICG, affording a higher tumor-detection rate (11). On the other hand, in vivo imaging in the NIR-IIb (1,500 to 1,700 nm) subwindow (19, 21, 27, 38, 39) demonstrated the highest image clarity (16) due to further suppressed light scattering and tissue autofluorescence (14). For example, molecular imaging of PD-L1 (programmed cell death ligand-1) in CT26 tumors in the 1,200- to 1,400-nm range afforded a T/NT ratio of ~9.5 using molecular fluorophore (31), higher than in the NIR-I window (T/NT ~2 to 3) (40), and drastically increased to T/NT ~40 in the NIR-IIb window using PD-L1 antibody conjugated to bright rare-earth down-conversion nanoparticles (21, 41). However, imaging-guided tumor-resection surgery in NIR-IIb has not been reported thus far.

Here, we developed a compact imager for simultaneous photographic imaging in the visible and fluorescence imaging in the NIR-I and NIR-II windows for intraoperative navigation of mouse tumor models under room light. We conjugated biocompatible erbium-based rare-earth nanoparticles (ErNPs) (21, 38) to TRC105 chimeric antibody for specific binding and molecular imaging of CD105 on tumor vasculatures (42, 43), affording a T/NT ratio of ~40 by imaging luminescence from ErNPs in the 1,500- to 1,700-nm NIR-IIb range under a 940-nm light-emitting diode (LED) at 30 mW/cm^2. During intraoperative surgery, ultra-high T/M ratios of ~300 were obtained, allowing precise tumor margin determination and cancer cell removal down to the few-cell level.

Results

A Visible Photographic and NIR-I/NIR-II Fluorescence Imager.
We built a portable imager by integrating a color camera for visible photography and a water-cooled indium gallium arsenide (InGaAs) camera for 900- to 1,700-nm fluorescence imaging (Fig. 1A and *Materials and Methods*). The two cameras used two imaging paths separated by a dichroic mirror and shared the same imaging lens sets to facilitate overlay of photographic and fluorescence images in real time. An 808-nm laser or a 940-nm LED (full width at half maximum [FWHM] ~76 nm; Fig. 1C, shaded curve) was used as excitation for the

fluorescence channel for IRDye800CW or ErNPs. Room light was used for illumination for colored photographic imaging through a 750-nm short-pass filter to block excitation light from the 808-nm laser or 940-nm LED. For concurrent photographic and NIR-I and NIR-II fluorescence imaging with IRDye800CW, a dichroic mirror with an 800-nm edge was used. A combination of a 900-nm long-pass filter and a 1,000-nm short-pass filter were used for NIR-I fluorescence collection in 900 to 1,000 nm, and a 1,100-nm long-pass filter and a 1,400-nm short-pass filter were employed for 1,100- to 1,400-nm imaging of IRDye800CW tail emission. For concurrent photographic and 1,500- to 1,700-nm imaging with ErNPs, a dichroic mirror with a 993-nm edge and a 1,500-nm long-pass filter were used for NIR-IIb fluorescence collection. A zoomable lens set with continuously variable magnifications (22 × 18 mm^2–44 × 34 mm^2) was used for large field-of-view (FOV) imaging and can be switched to a higher-resolution mode with a 5× objective (NA = 0.12, FOV: 5.8 × 4.7 mm^2). During imaging/surgery of mouse tumor, the room light was switched on, and either an 808-nm laser or a 940-nm LED was selected depending on the fluorescent probe. We used RGB (red, green, blue) LED for room lighting and observed that this type of room light had negligible influence on NIR-I and NIR-II fluorescence imaging (*SI Appendix*, Fig. S1).

Molecular Imaging of Tumors. TRC105 is a humanized clinical-stage monoclonal antibody to endoglin overexpressed on proliferating endothelial cells that has shown to specifically bind to vasculatures in human and murine tumors with high endoglin expression (42, 44) and has been used to treat human cancers (45, 46), murine CT26 colon tumor (47), and 4T1 breast tumor (48). It was also used in endoglin-based tumor imaging in mouse models (49, 50). For molecular imaging of angiogenesis in tumors, we conjugated TRC105 to a phase-I clinical trial fluorophore IRDye800CW or ErNPs to form IRDye800-antibody conjugate (IRDye800-TRC105) or ErNPs-antibody conjugate (ErNPs-TRC105) exhibiting bright down-conversion luminescence in the 1,500- to 1,700-nm NIR-IIb window developed by our group (Fig. 1B and *Materials and Methods*) (21, 38). The ErNPs were coated with three cross-linked hydrophilic polymeric layers (P^3 coating; *SI Appendix*) to impart biocompatibility in physiological environments and biliary excretion in ~2 wk without discernable toxic effects to mice (21, 41). The hydrodynamic size of ErNPs with P^3 coating was ~35.5 nm (21).

BALB/c mice were inoculated with 4T1 murine breast tumors on the left or right hindlimb and injected intravenously (i.v.) with IRDye800-TRC105 (~36 μg IRDye800CW per mouse) or ErNPs-TRC105 conjugates (typically ~2 mg ErNPs per mouse; down to 0.2 mg) through the tail vein. Whole-body fluorescence molecular imaging over time (Fig. 2A) was performed for mice injected with IRDye800-TRC105 i.v. under an 808-nm laser excitation at ~50 mW/cm^2 in the NIR-I (900 to 1,000 nm; Fig. 2 A, *Left*) and 1,100- to 1,400-nm ranges (Fig. 2 A, *Middle*). Like ICG, IRDye800CW exhibited an emission tail into the NIR-II window (51). However, emission almost diminished >1,300 nm, and NIR-II imaging with these dyes effectively detected 1,100- to 1,300-nm fluorescence using a 1,100-nm long-pass filter. With ErNPs-TRC105, 1,500- to 1,700-nm NIR-IIb molecular imaging of mice was excited by a 940-nm LED at 30 mW/cm^2.

Ten minutes post-injection (p.i.), IRDye800-TRC105 signal was observed all over mouse body (blood circulation half-time ~0.6 h; *SI Appendix*, Fig. S2), while ErNPs-TRC105 were
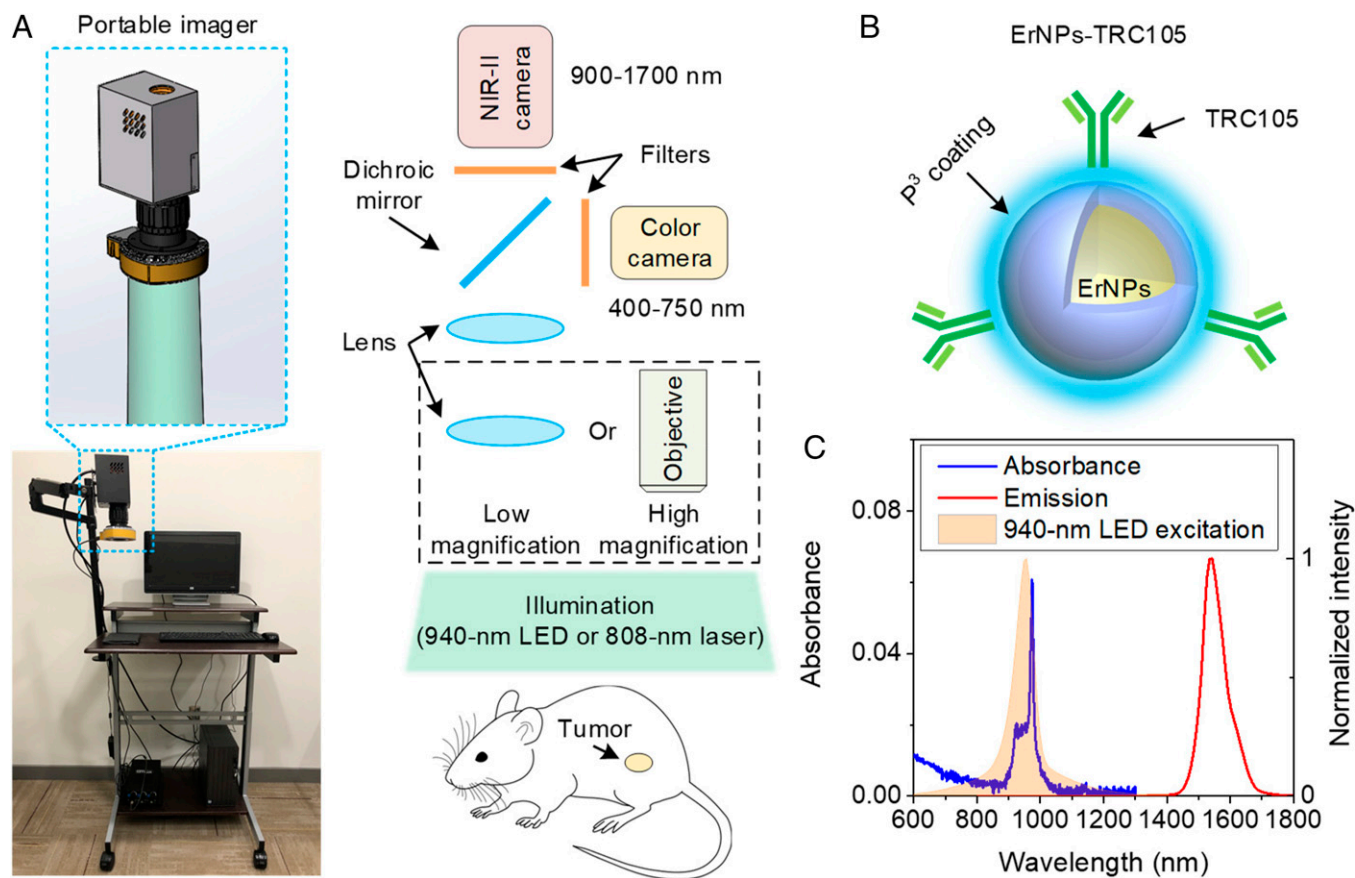
Fig. 1. The compact imager and contrast agent designed for image-guided surgery in the NIR-IIb window. (*A*) A photograph and a schematic of portable imager for simultaneous color and NIR-II imaging. A water-cooled NIR-II InGaAs camera and a color silicon camera were used in this imager. The front lens of the portable imager can be switched to an objective to realize high-resolution and magnification imaging. (*B*) Schematic design of NIR-IIb contrast agents by conjugating core-shell ErNPs with TRC105 antibody. A hydrophilic polymeric cross-linked network (P³ coating) was coated on the ErNPs to impart biocompatibility. The mass ratio of ErNPs and TRC105 antibody used in conjugation was ~6.7, and the estimated antibody per particle was ~1:2.5, assuming 50% conjugation efficiency. (*C*) Absorbance and emission spectra of P³-coated ErNPs and emission spectrum of the 940-nm LED.

mainly circulating in the blood vessels (Fig. 2*A* and *SI Appendix*, Fig. S3) with a blood circulation half-time of ~4 h. Over time, fluorescence signal in the 4T1 tumor increased for both IRDye800-TRC105 and ErNPs-TRC105, suggesting binding to the overexpressed CD105 on tumor vasculatures (52, 53). At 24 h p.i., mice injected with ErNPs-TRC105 showed a high tumor NIR-IIb emission signal with a low background signal over the body (5 ms exposure time), in contrast to the high background body signal for mice injected with IRDye800-TRC105 (Fig. 2*B*). A high T/NT ratio of ~40 was observed with ErNPs-TRC105, significantly ($P \leq 0.001$ based on Tukey's test, $n = 9$) higher than those with IRDye800-TRC105 ($n = 8$) recorded in the 900- to 1,000-nm NIR-I (T/NT ~4.4) and 1,100- to 1,300-nm NIR-II (T/NT ~5.9) windows (Fig. 2*C*). For mice injected with free ErNPs without antibody, we observed much lower T/NT ratios of ~10 (*SI Appendix*, Fig. S4) due to passive uptake through the enhanced permeability and retention (EPR) effect (54). Zeta potential values for free ErNPs and ErNPs-TRC105 were ~11.6 mV and ~6.3 mV, respectively.

To further demonstrate highly specific tumor targeting, we reduced the i.v. injection dose of ErNPs-TRC105 by an order of magnitude (to ~0.2 mg ErNPs per mouse) and still obtained excellent molecular imaging of CD105 in 4T1 tumors with a similar T/NT ratio of ~40 at 24 h p.i. (Fig. 2*C*; 200-ms exposure time). Fluorescence intensity of ErNPs-TRC105 in major organs, such as liver and spleen, gradually decreased over 2 wk,

and ex vivo NIR-IIb imaging of the major organs 2 wk p.i. detected negligible 1,500- to 1,700-nm emission, suggesting complete excretion of the contrast agents (*SI Appendix*, Figs. S5 and S6). Further histological results showed similar structures of major organs to healthy untreated control mice at 2 wk p.i. (*SI Appendix*, Fig. S7), without any discernable toxic effects caused by the ErNPs-TRC105 conjugates.

Intraoperative Navigation of Tumor Resection in Various Optical Windows. We performed image-guided surgery at 24 h p.i. for mice injected with IRDye800-TRC105 and ErNPs-TRC105 when the 4T1 tumors inoculated on mouse hindlimb reached ~4 to 8 mm. The fluorescence intensity of IRDye800CW in the 1,100- to 1,400-nm NIR-II window was weaker than that in the NIR-I window, requiring a 10-times-longer exposure time for NIR-II molecular imaging (20 ms vs. 2 ms). For targeted NIR-IIb imaging of 4T1 tumor with ErNPs-TRC105 (2 mg ErNPs per mouse), an exposure time of ~2 ms was used, allowing real-time intraoperative imaging at ~83 frames per second (fps). For color photographic imaging in the visible, the frame rate relied on room light intensity and was set to ~25 fps.

For imaging-guided surgery with IRDye800-TRC105, we first removed the skin covering the 4T1 tumor to expose the tumor and surrounding tissues (Fig. 3*A*, steps 1 and 2, and Movie S1). Imaging of IRDye800-TRC105 in both the NIR-I and the NIR-II windows observed substantial nonspecific body signals from the skin and tissues surrounding the tumor,
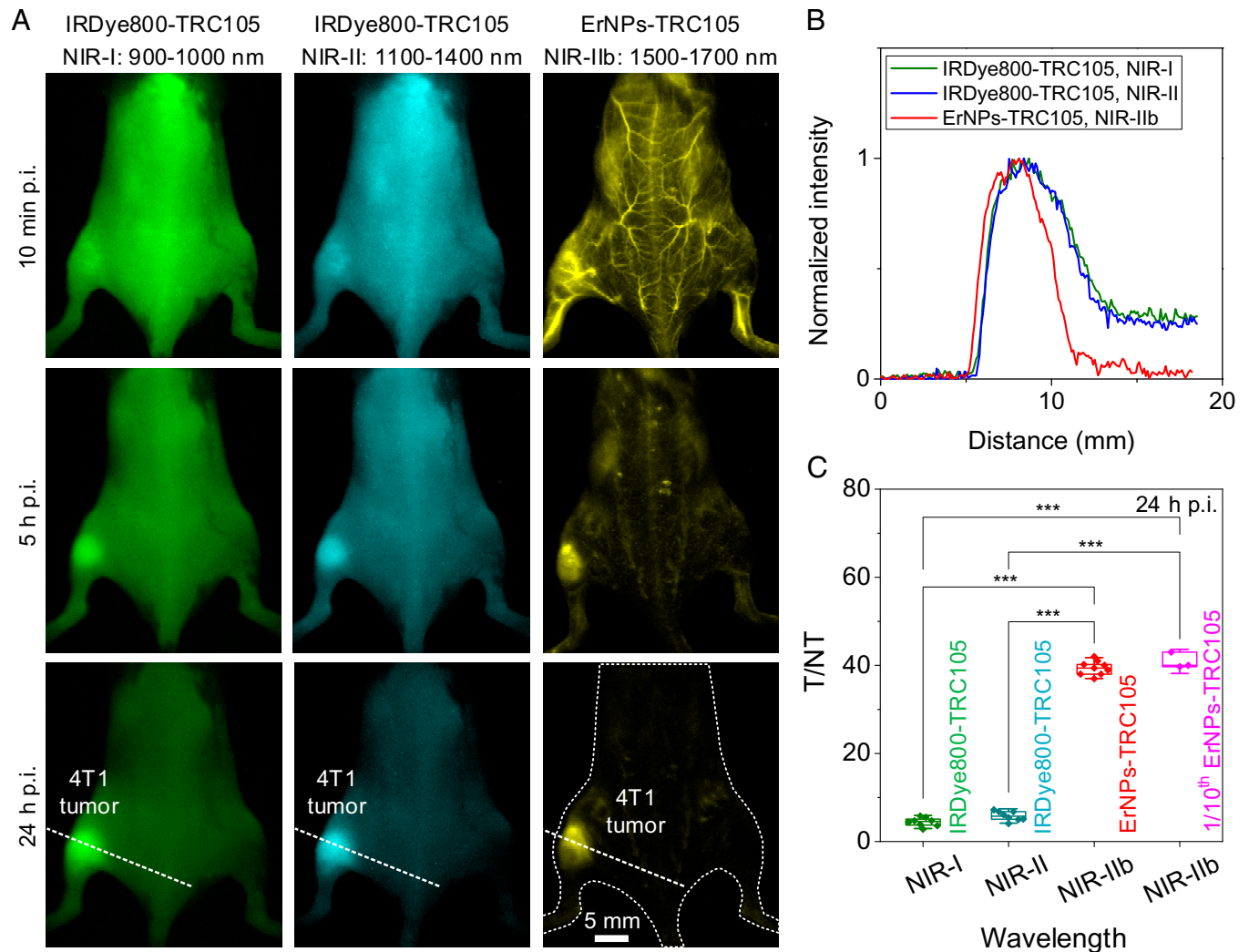
Fig. 2. In vivo molecular imaging of angiogenesis in 4T1 tumor in various NIR 900- to 1,700-nm subregions. (*A*) Fluorescence images of mice bearing a 4T1 tumor at different timepoints (10 min, 5 h, and 24 h p.i. as indicated) after i.v. injection of (*Left* and *Middle*) IRDye800-TRC105 or (*Right*) ErNPs-TRC105. The emission of IRDye800-TRC105 was collected in the NIR-I (900 to 1,000 nm) and NIR-II (1,100 to 1,400 nm) windows and excited by an 808-nm laser. ErNPs-TRC105 was excited by a 975-nm laser, and the emission was collected in the 1,500- to 1,700-nm window. The injection was performed through the tail vein when the tumor size reached ~4 to 8 mm (typically 3 to 6 d after inoculation). (*B*) Normalized intensity profiles along the dotted lines in *A*. (*C*) T/NT ratios of IRDye800-TRC105 ($n = 8$), ErNPs-TRC105 ($n = 9$), or 1/10th ErNPs-TRC105 ($n = 3$) at 24 h p.i. Data in *C* are presented as box plots (center line, median; inter-quartile range, 25th and 75th percentiles; whiskers, 1.5 × SD; points, outliers; ***$P \leq 0.001$, Tukey's test).

despite lower background in the NIR-II window than in NIR-I (Fig. 3 *A* and *B*). After skin removal, the underlying tumor and surrounding muscle showed T/M ratios of ~2.5 and ~3.6 in the NIR-I and NIR-II windows, respectively (Fig. 3*C*), slightly lower than T/NT ratios with the intact skin before surgery (NIR-I: T/NT = ~4.4, NIR-II: T/NT = ~5.9; Fig. 2*C*). The tumor margin was discerned over the background, but contrast was low (see two images of different magnification in step 2 of Fig. 3*A*). After the main tumor was removed, the tumor bed, surrounding skin, and muscle tissues still showed high background fluorescence emission, making it difficult to discern tumor residues with high confidence (step 3 in Fig. 3*A* and Movie S2).

Next, we performed imaging-guided 4T1 tumor resection surgery in the 1,500- to 1,700-nm NIR-IIb window using ErNPs-TRC105 as the tumor-targeting probe 24 h p.i. Visible photographic and NIR-IIb luminescence images of the 4T1 tumor overlaid very well (step 1 in Fig. 4*A*), with a T/NT ~40 (Fig. 2*C*). After resecting the skin covering the tumor and surrounding tissues (Movie S3), we observed the ErNPs-TRC105-targeted tumor lesion exhibited much stronger NIR-IIb fluorescence than the peripheral muscles with a T/M ~300

(step 2 in Fig. 4*A* and Movies S4 and S5), significantly ($P \leq$ 0.001, $n = 5$, Tukey's test; *SI Appendix,* Fig. S8) higher compared to the T/M of ~4 to 6 afforded by IRDye800-TRC105-based ($n = 6$) NIR-I and NIR-II imaging (Step 2 in Fig. 3*A*). The higher T/M ratio of ~300 (Fig. 4*C*) than T/NT ~40 (Fig. 2*C*) upon skin removal suggested skin uptake of the ErNPs-TRC105 probes to an extent. NIR-IIb imaging of the ErNPs-TRC105 probes detected bright signals in the tumor with much sharper signal changes (to near zero) at the edge of the tumor (Fig. 4*B*) than NIR-I and NIR-II imaging of IRDye800-TRC105, greatly improving tumor margin assessment (see images recorded in step 2 in Fig. 4*A* at two different magnifications). Sometimes, we observed stronger signal of ErNPs-TRC105 in the peritumoral region than in the middle area of the tumor (Fig. 4*A*), but this was not always the case (*SI Appendix,* Fig. S9). The distribution of ErNPs-TRC105 in the tumor reflected the spatial distribution of endoglin overexpressed on proliferating endothelial cells in the 3D structures of tumor vasculatures, which appeared to be highly variable between tumors and mice. After tumor removal, we sliced the tumor to make thin sections for hematoxylin and eosin (H&E)
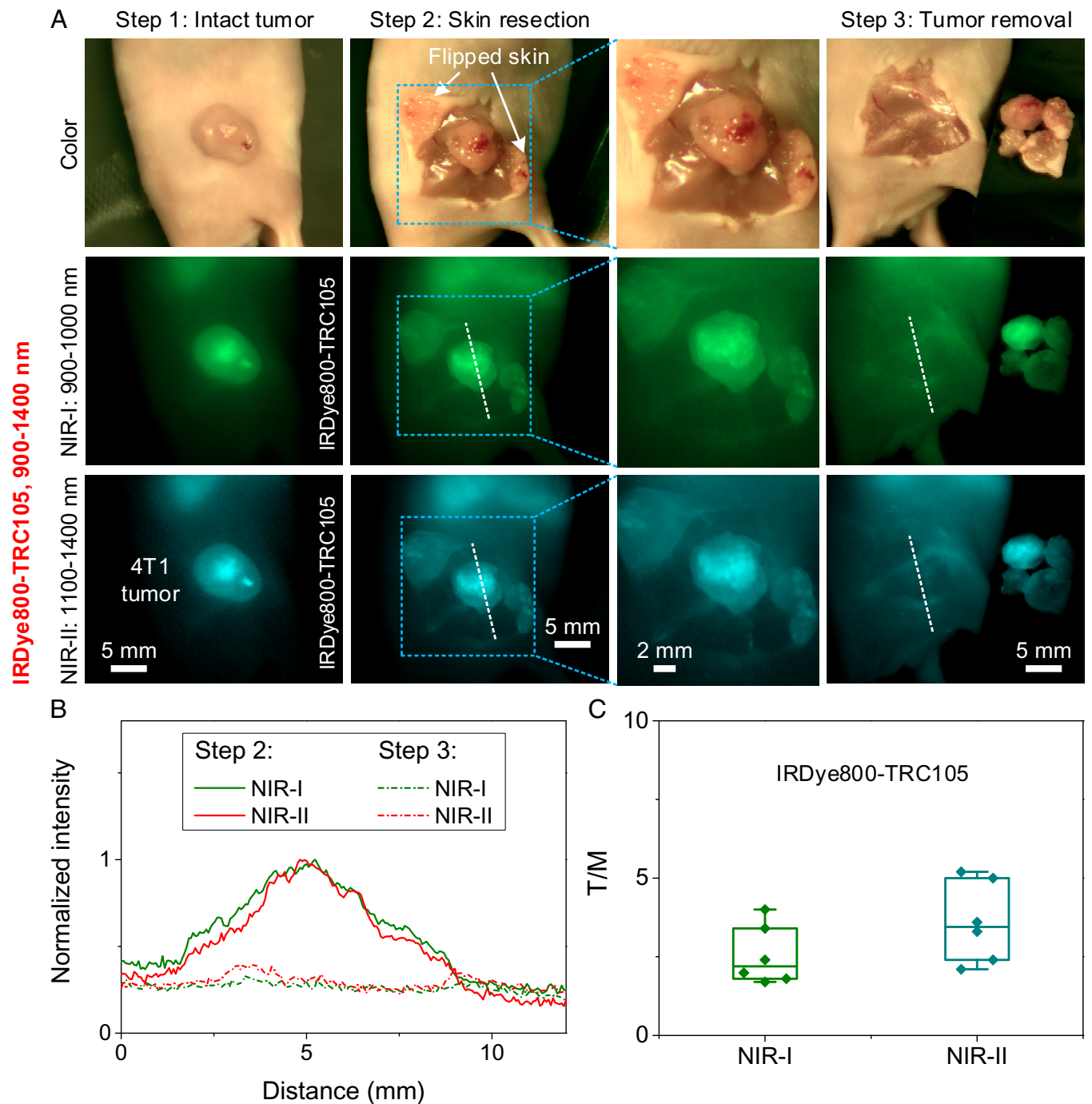
Fig. 3. Image-guided surgery in the visible and NIR-I or NIR-II windows. (*A*) (*Upper*) Color/visible imaging recorded during surgery. NIR-I fluorescence imaging (*Middle*) and NIR-II fluorescence imaging (*Lower*) of 4T1 tumor removal 24 h after i.v. injection of IRDye800-TRC105. Fluorescence was excited by an 808-nm laser. NIR-I and NIR-II emissions were collected in the 900- to 1,000-nm and 1,100- to 1,400-nm windows, respectively. The skin covering the tumor was resected initially to expose the tumor, and then the tumor was removed step by step. The largest FOV (44 × 34 mm^2) of the zoomable lens set was used to guide surgery (step 1 to step 3). The tumor area marked by a rectangle in step 2 was locally magnified using the highest magnification (FOV: 22 × 18 mm^2) of the zoomable lens set. (*B*) Normalized intensity profiles along the dotted lines in *A*. A strong body signal was left after tumor removal 24 h p.i. of IRDye800-TRC105. (*C*) T/M ratios of IRDye800-TRC105 in NIR-I and NIR-II windows. T/M ratios were calculated using the fluorescence intensity of tumor and muscle measured after skin resection (step 2 in *A*). Data in *C* are presented as box plots (center line, median; interquartile range, 25th and 75th percentiles; whiskers, 1.5 × SD; points, outliers).

staining/photographic imaging and NIR-IIb fluorescence imaging of the same regions near the tumor–normal tissue boundaries (see Fig. 4*D* and *SI Appendix*, Fig. S10 for details). Overlaying the H&E and NIR-IIb images showed that ErNPs-TRC105 signals were, indeed, detected in H&E-stained tumor regions and rarely in normal tissue regions (Fig. 4*D* and *SI Appendix*, Fig. S10).

Upon removing the bulk of the tumor guided by NIR-IIb imaging (step 3 in Fig. 4*A*), we used the highest magnification

of the zoomable lens set (by adjusting the zoomable lens set to reach a FOV of ∼22 × 18 mm^2) to examine any residual fluorescence signal associated with leftover tumor lesions (Fig. 5*A*). For resected 4T1 tumor residues labeled by ErNPs-TRC105 imaged in NIR-IIb, we sometimes observed small bright fluorescence spots in the NIR-IIb window well above the ∼0 background (Fig. 5*A*). We then switched to the high-resolution mode equipped with a 5× objective (NA = 0.12) for
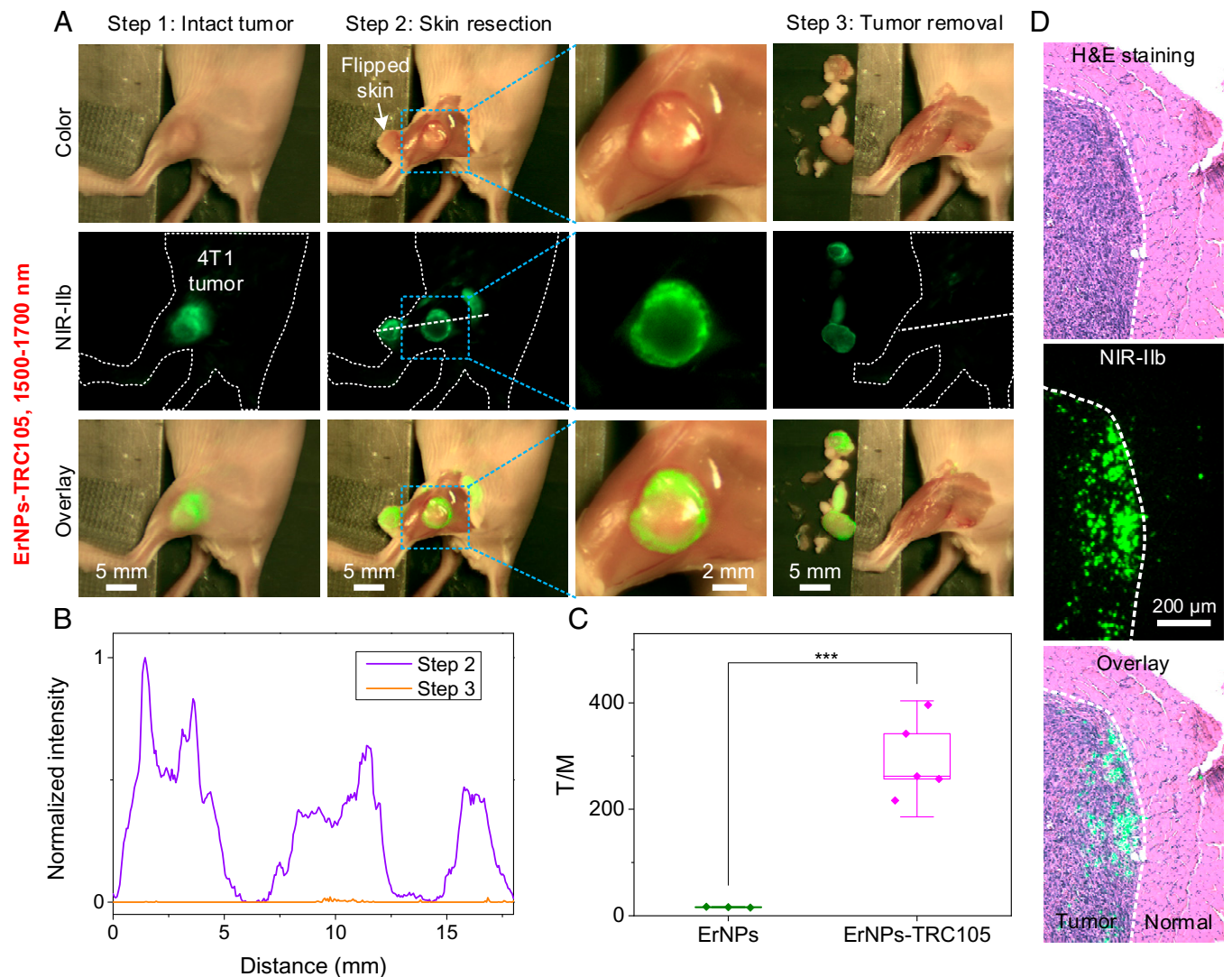
Fig. 4. Molecular image-guided surgery in the visible and NIR-IIb windows. (*A*) 4T1 tumor removal guided by the observation in the visible (*Upper*) and NIR-IIb (*Middle*) windows 24 h p.i. of ErNPs-TRC105. Fluorescence was excited by a 940-nm LED. NIR-IIb emission was collected in the 1,500- to 1,700-nm window. (*Lower*) Overlay images of color and NIR-IIb molecular fluorescence images. Image-guided surgery was navigated by the zoomable lens set with a FOV of 44 × 34 mm². Tumor margin was analyzed in step 2 using the same zoomable lens set with a FOV of 22 × 18 mm². (*B*) Normalized intensity profiles along the dotted lines in *A*. (*C*) T/M ratios of free ErNPs and ErNPs-TRC105 in NIR-IIb window. Data in *C* are presented as box plots (center line, median; interquartile range, 25th and 75th percentiles; whiskers, 1.5 × SD; points, outliers; ***$P \leq 0.001$, Tukey's test). (*D*) Two channel (*Upper*) H&E and (*Middle*) NIR-IIb imaging of tumor slices resected 24 h p.i. of ErNPs-TRC105 (see *SI Appendix*, Fig. S10 for experimental details). Note that the tumor slices were ultrathin (~5 μm) and did not contain large numbers of ErNPs-TRC105 in each slice.

NIR-IIb molecular imaging and observed small tumor residues containing thousands of cells (~400 μm × 850 μm in size in Fig. 5*C*), resolving down to tens of microns features on the order of several cancer cell dimensions (~38 μm features in Fig. 5 *A–D*). Guided by such imaging, we excised the NIR-IIb emitting small residue lesions labeled by ErNPs-TRC105 (Movie S6) until no ErNPs-TRC105 signal was observed in the original tumor area (Fig. 5*E*), completing surgical removal of tumor down to the cellular level. For resected 4T1 tumor residues labeled by IRDye800-TRC105 imaged in the NIR-I and NIR-II windows, we observed only featureless background signals under high-resolution mode (*SI Appendix*, Fig. S11) and were unable to identify and remove small residual tumor lesions.

Discussion

NIR imaging-guided surgery has attracted much attention due to the potential of revolutionizing oncological cancer surgery (1). Preclinical and clinical trials have been pursued using

biocompatible fluorophores (ICG-like dyes, IRDye800CW, and ZW800) and FDA-approved instruments (1, 2, 12, 55, 56). An example is IRDye800CW-based molecular imaging in both preclinical and clinical settings, with a caveat of peripheral tissues around tumor showing strong background signals, leading to low tumor-to-background ratios <5 and blurred tumor margin (13, 57–59) and consistent with our current finding with IRDye800-TRC105 (Fig. 3). NIR-II imaging has shown improved penetration depth and lower background due to suppressed light scattering and tissue autofluorescence. Indeed, by utilizing the tail emission of ICG-like dyes in the NIR-II window, clinical trials were performed in the short-wavelength range (~1,000 to 1,300 nm) of the NIR-II window for ~2× improved T/NT ratio (37), in addition to preclinical NIR-II imaging-guided tumor resection and sentinel lymph node mapping (26, 35, 60, 61). Despite this progress, we found that improvements to T/NT ~5.9 and T/M ~3.6 with the ICG-like IRDye800CW were insufficient to eliminate nonspecific background signal or boost tumor margin resolution (Fig. 3).
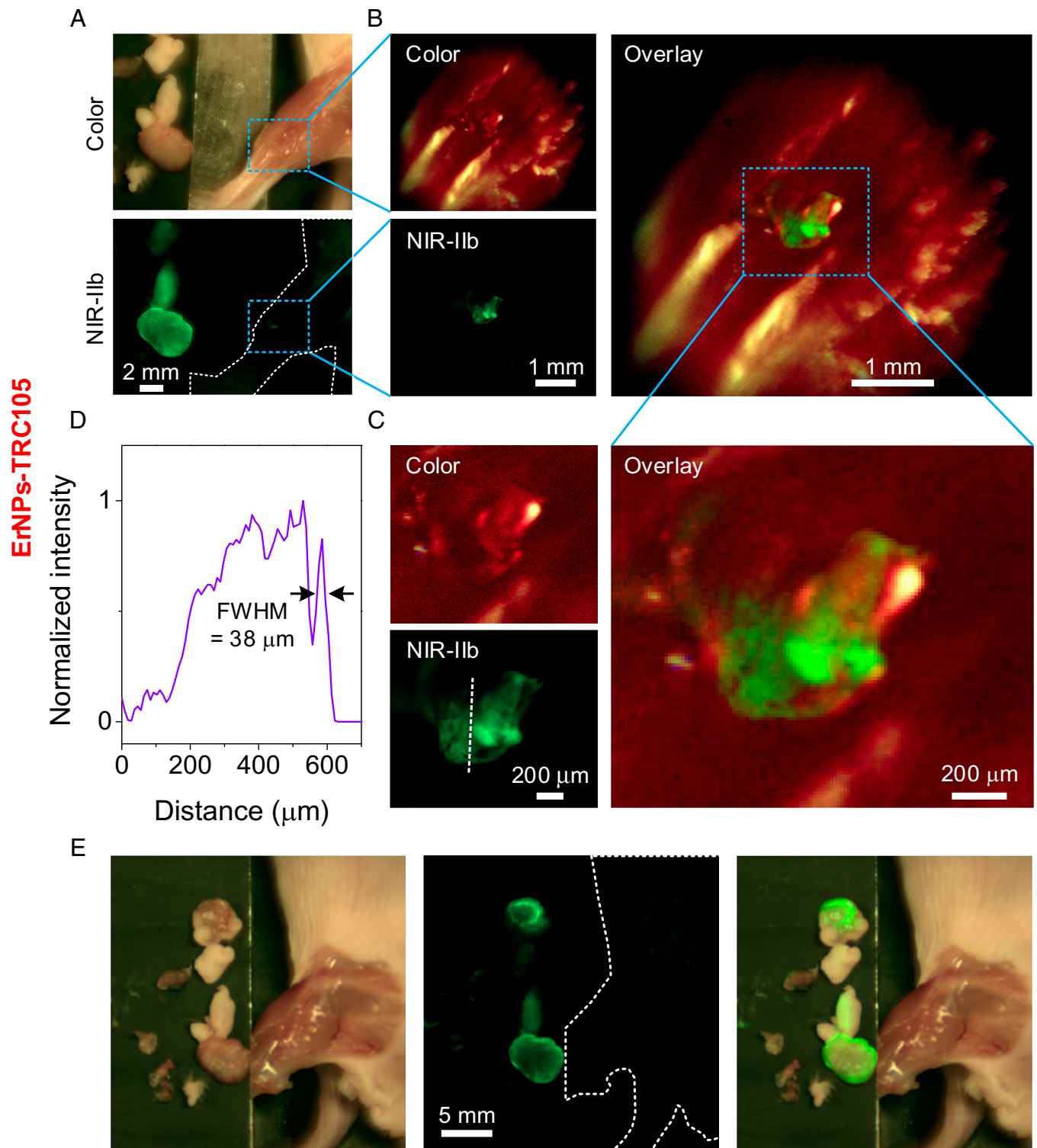
Fig. 5. Residual tumor fragments' precise removal navigated by our portable imager with high magnification and resolution. (*A*) Color and NIR-IIb imaging of the surgery area after tumor removal observed by the highest magnification of the zoomable lens set with a FOV of 22×18 mm^2. When the 4T1 tumor size reached ~4 to 8 mm (typically 3 to 6 d after inoculation), ErNPs-TRC105 was injected i.v. The surgery was performed 24 h p.i. (*B*) High-magnification imaging resolved a small residual tumor fragment after main tumor removal, performed by replacing the front lens of zoomable lens with a 5× objective (NA = 0.12, FOV: 5.8×4.7 mm^2). (*C*) High-magnification imaging of the rectangular highlighted region in *B*. (*D*) A normalized intensity profile along the dotted line in *C* revealing structures with a feature size of 38 μm. (*E*) Low-magnification imaging of surgery area using zoomable lens set with a FOV of 44×34 mm^2 after tumor removal under high-resolution view.

With the targeted NIR-IIb probes of ErNPs-TRC105, 1 to 2 orders of improvements were afforded (T/NT ratios of ~40 and T/M ~300; Figs. 2 and 4), allowing for unambiguous tumor margin identification and thorough tumor removal down to the few-cell level (Figs. 4 and 5).

In general, in vivo fluorescence imaging in the 1,000- to 1,700-nm window can improve tissue penetration depth, signal-to-background ratio, and spatial resolution over the traditional 800- to 900-nm NIR-I window. However, we believe that imaging only in the 1,500- to 1,700-nm NIR-IIb

subwindow represents a true breakthrough since light scattering is minimized and tissue autofluorescence reduces to zero (i.e., noise level) due to a vast Stoke's shift from <1,000-nm excitation (19, 21, 27, 38). Our current work again confirmed these findings, observing noise level background signals on healthy tissues free of any ErNP probes. Any NIR-IIb emission should be from the engineered probes intended for specific tumor targeting. In this regard, the precision of NIR-IIb imaging-guided surgery will also hinge on the efficiency and specificity of targeting ligands on the probes in order to achieve ~100% labeling of cancerous tissues without mislabeling. High T/NT (>30 to 40) and T/M ratios (>100) are desired and could be assuring of targeting efficacy.

The ErNPs-TRC105 probes exhibited negligible nonspecific uptake by healthy tissues in vivo due to the stealth nature of the cross-linked P^3 hydrophilic polymer coating on the ErNPs (41). The P^3-coated ErNPs conjugated to TRC105 antibody circulated in the blood vasculatures with a blood circulation half-time of ~4 h, allowing continuous binding of the ErNPs specifically to CD105 overexpressed on tumor. In contrast, IRDye800-TRC105 was observed all over the body 10 min p.i. with a shorter blood circulation half-time of ~0.6 h and strong body background fluorescence even after skin removal due to nonspecific binding or uptake of the dye-antibody complexes by normal tissues (12).

The highly cross-linked nature of P^3 polymeric coating on nanoparticles imparted high biocompatibility of various NIR-II imaging probes—including quantum dots, ErNPs, and magnetic particles—preventing the functionalization layer on nanoparticles from detaching in vivo (41). The P^3-coated ErNPs were fully excreted from the body within 2 wk of i.v. injection without causing toxic side effects shown here and previously (21), making these down-conversion NIR-IIb probes promising for clinical translation. It was encouraging that the 1/10 dose of ErNPs-TRC105 at the ~8 mg/kg level allowed for excellent molecular imaging of tumor with a T/NT ratio ~40 at 24 h p.i. Such a dose was reasonably low, considering the 0.5 to 1.6 mg/kg doses typically used for the much lower molar mass IRDye800CW (57, 58).

For future clinical translation, it is important to build imaging systems for visible photographic and NIR-II fluorescence/luminescence imaging for imaging guided surgery, especially in the presence of bright room light. We designed a compact imager to detect the range of 400 to 1,700 nm using a widely available silicon complementary metal–oxide–semiconductor camera (color photographic imaging) and an InGaAs camera (NIR-II imaging) with a high quantum efficiency of >80% in the NIR-IIb window capable of high detection sensitivity for NIR-IIb labels such as ErNPs. The two cameras shared the same lens sets for overlaying colored photographic and NIR-II images in real time, facilitating intraoperative navigation during surgery. We found it highly useful to image at variable magnifications to span the centimeter-to-submillimeter scales and to guide tumor resection down to a few cells without leaving residues while preventing overcutting. It was also interesting that we found that among various lighting conditions tested, a particular type of room lighting based on RGB-LED (*Materials and Methods*) allowed excellent visual inspections and visible photographic imaging during surgery, without giving discernible background signals in the NIR-IIb range to degrade fluorescence/luminescence imaging. This is important to meet a requirement for potential clinic use of optical imaging-guided surgery. Previous NIR-I fluorescence imaging required room lighting to be dimmed or switched off or transient lighting

methods switching from fluorescence collection to room lighting at a high frequency (3, 11).

Fluorescence imaging has been explored for surgical navigation for many years. The ultra-high signal-to-background contrast enabled by molecular imaging in the NIR-IIb 1,500- to 1,700-nm window can afford orders-of-magnitude-higher ability in distinguishing malignant and healthy tissues than previous approaches. It is foreseeable to scale up the biocompatible rare-earth nanoparticles, identify the optimal targeting ligands and conjugation chemistry, and develop clinically compatible imaging systems. This could open a paradigm of molecular imaging-guided surgery for clinical use.

Materials and Methods

Materials. The cubic-phase ErNPs with P^3 coating used in this work were prepared according to our previous work (21) with details provided in *SI Appendix*. IRDye800CW NHS Ester was purchased from LI-COR. TRC105 was provided by TRACON Pharmaceuticals. 1-(3-dimethylaminopropyl)-3-ethylcarbodiimide hydrochloride (EDC) was purchased from Sigma-Aldrich.

Conjugation of TRC105 to IRDye800CW. IRDye 800CW was dissolved in dimethyl sulfoxide at a concentration of 4 mg/mL. Nine microliters IRDye 800CW, 300 µg TRC105 (in 500 µL PBS buffer), and 100 µL dipotassium phosphate (1 M in water) were mixed with a dye-to-protein ratio of 18.7:1, and the solution was shaken at room temperature in the dark for 3 h. The solution was washed with a 10-k centrifugal filter five times to remove excess IRDye800CW and then dispersed in 200 µL 1 × PBS solution for further injection. The dye-to-antibody ratio in the final conjugate was ~2.7:1, measured by the dye vendor's protocol (62).

Conjugation of TRC105 to P^3-Coated ErNPs (ErNPs-TRC105). In total, 2 mg P^3-coated ErNPs, TRC105 (300 µg), EDC (1.5 mg), and 800-µL 4-Morpholineethanesulfonic acid [2-(N-Morpholino)ethanesulfonic acid hydrate] solution (10 mM, pH = 11) were mixed and shaken at room temperature for 3 h. The solution was first centrifuged at 4,400 rpm for 30 min to remove potential large floccules. Then, the supernatant was washed by centrifuge filter (100 kDa) four times and dispersed in 200 µL 1 × PBS solution for further use.

Imaging System for Intraoperative Navigation. Two cameras were integrated in the compact imager. A silicon camera (# 33-981, Edmund Optics Inc.) was used for color imaging, and a water-cooled InGaAs camera (Ninox 640 II, Raptor Photonics) with spectral response in the window of 400 to 1,700 nm was used for NIR-I or NIR-II imaging. The lens set for large FOV was composed of two achromatic lenses (AC508-100-C, AC508-1000-C, Thorlabs). A 5× objective (NA = 0.12, Leica N Plan) was used for high-resolution imaging. An 808-nm laser (MDL-H-808, Changchun New Industries Tech. Co., Ltd.) and a 940-nm LED (EFFI-RING-940-SD-P3, CCS America, Inc.) were used to excite NIR-I or NIR-II dyes. The 940-nm LED was filtered by 1,250-nm short-pass filters (#84-657, Edmund Optics Inc.) to make the excitation clean in the NIR-IIb window. An RGB-based LED room light (EPANL LED Flat Panel, Lithonia Lighting) was used for room lighting and as light source for color imaging. A 750-nm short-pass filter (FESH0750, Thorlabs) was applied before the color camera. Two dichroic mirrors (Di03-R785-t1, Di02-R980, Semrock) were selected to be used in our experiments for visible and NIR-I imaging or visible and NIR-II imaging. A 900-nm long-pass filter (FELH0900, Thorlabs) and a 1,000-nm short-pass filter (FESH1000, Thorlabs) were used for NIR-I imaging. A 1,100-nm long-pass filter (FELH1100, Thorlabs) and a 1,400-nm short-pass filter (#84-652, Edmund Optics Inc.) were used for NIR-II imaging. A 1,500-nm long-pass filter (FELH1500, Thorlabs) was used for NIR-IIb imaging.

Data Processing. The FWHM was measured in OriginLab 9.0. The SD and mean were calculated by OriginLab 9.0. The Tukey's test was performed in OriginLab (2021).

Mouse Handling and Tumor Inoculation. Mouse handling was approved by Stanford University's administrative panel on Laboratory Animal Care. All experiments were performed according to the NIH *Guide for the Care and Use of*

Laboratory Animals (63). BALB/c female mice were purchased from Charles River. Bedding, nesting material, food, and water were provided. The 6-wk-old BALB/c mice were shaved using hair remover lotion (Nair, Softening Baby Oil) and inoculated with ~1 million 4T1 cancer cells for single tumor on the left or right hindlimb. Mice were randomly selected from cages for all experiments. During shaving or imaging, all mice were anesthetized by a rodent anesthesia machine with 2 L min^{-1} O$_2$ gas mixed with 3% isoflurane.

In Vivo Wide-Field Fluorescence Imaging. For time-course imaging of mice injected with 200-μL ErNPs-TRC105 (10 mg/mL) or 200-μL IRDye800-TRC105 (0.08 mg/mL), the NIR-I, NIR-II, and NIR-IIb wide-field fluorescence images were recorded by a 2D water-cooled InGaAs camera (Ninox 640, Raptor Photonics) working at −21°C. The fluorescence signal was collected by two achromatic lenses to the camera after being filtered by corresponding filters, as discussed in the previous content. An 808-nm and a 975-nm laser were used to excite IRDye800-TRC105 and ErNPs-TRC105, respectively, with actual power intensity of ~50 mW/cm^2.

Image-Guided Surgery Using Portable Imager. The 200-μL ErNPs-TRC105 (10 mg/mL) or 200-μL IRDye800-TRC105 (0.08 mg/mL) were injected i.v. into

mice bearing 4T1 tumors as tumor size reached ~4 to 8 mm (typically 3 to 6 d after inoculation). Then, 24 h p.i., the surgery was performed with navigation provided by portable imager in visible and NIR-I/NIR-II windows. Mice injected with IRDye800-TRC105 were excited by an 808-nm laser with a power intensity of ~50 mW/cm^2, and fluorescence was collected in the NIR-I (900 to 1,000 nm) and NIR-II (1,100 to 1,400 nm) windows by selecting corresponding optical filter combinations. NIR-IIb molecular imaging of mice injected with ErNPs-TRC105 was excited by a 940-nm LED with a power intensity of 30 mW/cm^2. Room light was used for color image. After surgery, the mice were euthanized.

Data Availability. All study data are included in the article and/or supporting information.

Author affiliations: [a]Department of Chemistry, Stanford University, Stanford, CA 94305; [b]Bio-X, Stanford University, Stanford, CA 94305; and [c]School of Medicine, Stanford University, Stanford, CA 94303

1. A. L. Vahrmeijer, M. Hutteman, J. R. van der Vorst, C. J. H. van de Velde, J. V. Frangioni, Image-guided cancer surgery using near-infrared fluorescence. *Nat. Rev. Clin. Oncol.* **10**, 507–518 (2013).
2. S. Hernot, L. van Manen, P. Debie, J. S. D. Mieog, A. L. Vahrmeijer, Latest developments in molecular tracers for fluorescence image-guided cancer surgery. *Lancet Oncol.* **20**, e354–e367 (2019).
3. R. R. Zhang *et al.*, Beyond the margins: Real-time detection of cancer using targeted fluorophores. *Nat. Rev. Clin. Oncol.* **14**, 347–364 (2017).
4. L. E. McCahill *et al.*, Variability in reexcision following breast conservation surgery. *JAMA* **307**, 467–475 (2012).
5. M. A. Stammes *et al.*, Modalities for image- and molecular-guided cancer surgery. *Br. J. Surg.* **105**, e69–e83 (2018).
6. G. Hong, A. L. Antaris, H. Dai, Near-infrared fluorophores for biomedical imaging. *Nat. Biomed. Eng.* **1**, 10 (2017).
7. S. L. Troyan *et al.*, The FLARE intraoperative near-infrared fluorescence imaging system: A first-in-human clinical trial in breast cancer sentinel lymph node mapping. *Ann. Surg. Oncol.* **16**, 2943–2952 (2009).
8. J. R. van der Vorst *et al.*, Near-infrared fluorescence-guided resection of colorectal liver metastases. *Cancer* **119**, 3411–3418 (2013).
9. E. Tanaka *et al.*, Real-time assessment of cardiac perfusion, coronary angiography, and acute intravascular thrombi using dual-channel near-infrared fluorescence imaging. *J. Thorac. Cardiovasc. Surg.* **138**, 133–140 (2009).
10. N. J. Harlaar *et al.*, Molecular fluorescence-guided surgery of peritoneal carcinomatosis of colorectal origin: A single-centre feasibility study. *Lancet Gastroenterol. Hepatol.* **1**, 283–290 (2016).
11. Z. Hu *et al.*, First-in-human liver-tumour surgery guided by multispectral fluorescence imaging in the visible and near-infrared-I/II windows. *Nat. Biomed. Eng.* **4**, 259–271 (2020).
12. H. S. Choi *et al.*, Targeted zwitterionic near-infrared fluorophores for improved optical imaging. *Nat. Biotechnol.* **31**, 148–153 (2013).
13. A. B. Morlandt *et al.*, Fluorescently labeled cetuximab-IRDye800 for guided surgical excision of Ameloblastoma: A proof of principle study. *J. Oral Maxillofac. Surg.* **78**, 1736–1747 (2020).
14. S. Diao *et al.*, Biological imaging without autofluorescence in the second near-infrared region. *Nano Res.* **8**, 3027–3034 (2015).
15. K. Welsher *et al.*, A route to brightly fluorescent carbon nanotubes for near-infrared imaging in mice. *Nat. Nanotechnol.* **4**, 773–780 (2009).
16. F. Wang *et al.*, Non-invasive confocal fluorescence imaging of mice beyond 1700 nm using superconducting nanowire single-photon detectors. bioRxiv [Preprint] (2021). https://www.biorxiv.org/content/10.1101/2021.08.13.456312v1 (Accessed 20 October 2021).
17. Q. Yang *et al.*, Donor engineering for NIR-II molecular fluorophores with enhanced fluorescent performance. *J. Am. Chem. Soc.* **140**, 1715–1724 (2018).
18. Y. Li *et al.*, Design of AIEgens for near-infrared IIb imaging through structural modulation at molecular and morphological levels. *Nat. Commun.* **11**, 1255 (2020).
19. M. Zhang *et al.*, Bright quantum dots emitting at ~1,600 nm in the NIR-IIb window for deep tissue fluorescence imaging. *Proc. Natl. Acad. Sci. U.S.A.* **115**, 6590–6595 (2018).
20. O. T. Bruns *et al.*, Next-generation in vivo optical imaging with short-wave infrared quantum dots. *Nat. Biomed. Eng.* **1**, 56 (2017).
21. Y. Zhong *et al.*, In vivo molecular imaging for immunotherapy using ultra-bright near-infrared-IIb rare-earth nanoparticles. *Nat. Biotechnol.* **37**, 1322–1331 (2019).
22. Y. Fan *et al.*, Lifetime-engineered NIR-II nanoparticles unlock multiplexed in vivo imaging. *Nat. Nanotechnol.* **13**, 941–946 (2018).
23. D. J. Naczynski *et al.*, Rare-earth-doped biological composites as in vivo shortwave infrared reporters. *Nat. Commun.* **4**, 2199 (2013).
24. F. Wang *et al.*, Light-sheet microscopy in the near-infrared II window. *Nat. Methods* **16**, 545–552 (2019).
25. F. Wang *et al.*, In vivo NIR-II structured-illumination light-sheet microscopy. *Proc. Natl. Acad. Sci. U.S.A.* **118**, e2023888118 (2021).
26. R. Tian *et al.*, Multiplexed NIR-II probes for lymph node-invaded cancer detection and imaging-guided surgery. *Adv. Mater.* **32**, e1907365 (2020).
27. S. Diao *et al.*, Fluorescence imaging in vivo at wavelengths beyond 1500 nm. *Angew. Chem. Int. Ed. Engl.* **54**, 14758–14762 (2015).
28. G. Hong *et al.*, Through-skull fluorescence imaging of the brain in a new near-infrared window. *Nat. Photonics* **8**, 723–730 (2014).
29. G. Hong *et al.*, Multifunctional in vivo vascular imaging using near-infrared II fluorescence. *Nat. Med.* **18**, 1841–1846 (2012).
30. A. L. Antaris *et al.*, A small-molecule dye for NIR-II imaging. *Nat. Mater.* **15**, 235–242 (2016).
31. H. Wan *et al.*, Developing a bright NIR-II fluorophore with fast renal excretion and its application in molecular imaging of immune checkpoint PD-L1. *Adv. Funct. Mater.* **28**, 1804956 (2018).
32. H. Wan, H. Du, F. Wang, H. Dai, Molecular imaging in the second near-infrared window. *Adv. Funct. Mater.* **29**, 1900566 (2019).
33. X. Zhang *et al.*, A thiopyrylium salt for PET/NIR-II tumor imaging and image-guided surgery. *Mol. Oncol.* **14**, 1089–1100 (2020).
34. H. Zhou *et al.*, Specific small-molecule NIR-II fluorescence imaging of osteosarcoma and lung metastasis. *Adv. Healthc. Mater.* **9**, e1901224 (2020).
35. P. Wang *et al.*, NIR-II nanoprobes in-vivo assembly to improve image-guided surgery for metastatic ovarian cancer. *Nat. Commun.* **9**, 2898 (2018).
36. P. Wang *et al.*, Downshifting nanoprobes with follicle stimulating hormone peptide fabrication for highly efficient NIR II fluorescent bioimaging guided ovarian tumor surgery. *Nanomedicine (Lond.)* **28**, 102198 (2020).
37. J. A. Carr *et al.*, Shortwave infrared fluorescence imaging with the clinically approved near-infrared dye indocyanine green. *Proc. Natl. Acad. Sci. U.S.A.* **115**, 4465–4470 (2018).
38. Y. Zhong *et al.*, Boosting the down-shifting luminescence of rare-earth nanocrystals for biological imaging beyond 1500 nm. *Nat. Commun.* **8**, 737 (2017).
39. C. Sun *et al.*, J-aggregates of cyanine dye for NIR-II in vivo dynamic vascular imaging beyond 1500 nm. *J. Am. Chem. Soc.* **141**, 19221–19225 (2019).
40. S. Chatterjee *et al.*, A humanized antibody for imaging immune checkpoint ligand PD-L1 expression in tumors. *Oncotarget* **7**, 10215–10227 (2016).
41. Z. Ma *et al.*, Cross-link-functionalized nanoparticles for rapid excretion in nanotheranostic applications. *Angew. Chem. Int. Ed. Engl.* **59**, 20552–20560 (2020).
42. A. Brossa, L. Buono, B. Bussolati, Effect of the monoclonal antibody TRC105 in combination with Sunitinib on renal tumor derived endothelial cells. *Oncotarget* **9**, 22680–22692 (2018).
43. E. Fonsatti, M. Maio, Highlights on endoglin (CD105): From basic findings towards clinical applications in human cancer. *J. Transl. Med.* **2**, 18 (2004).
44. C. R. Mehta, L. Liu, C. Theuer, An adaptive population enrichment phase III trial of TRC105 and pazopanib versus pazopanib alone in patients with advanced angiosarcoma (TAPPAS trial). *Ann. Oncol.* **30**, 103–108 (2019).
45. A. B. Apolo *et al.*, A phase II clinical trial of TRC105 (anti-endoglin antibody) in adults with advanced/metastatic urothelial carcinoma. *Clin. Genitourin. Cancer* **15**, 77–85 (2017).
46. C. R. Mehta, L. Liu, C. Theuer, An adaptive population enrichment phase III trial of TRC105 and pazopanib versus pazopanib alone in patients with advanced angiosarcoma (TAPPAS trial). *Ann. Oncol.* **30**, 103–108 (2019).
47. M. Tsujie *et al.*, Anti-tumor activity of an anti-endoglin monoclonal antibody is enhanced in immunocompetent mice. *Int. J. Cancer* **122**, 2266–2273 (2008).
48. H. Tian *et al.*, Endoglin interacts with VEGFR2 to promote angiogenesis. *FASEB J.* **32**, 2934–2949 (2018).
49. L. Karmani *et al.*, Biodistribution of (125)I-labeled anti-endoglin antibody using SPECT/CT imaging: Impact of in vivo deiodination on tumor accumulation in mice. *Nucl. Med. Biol.* **43**, 415–423 (2016).
50. H. Luo *et al.*, Dual targeting of tissue factor and CD105 for preclinical PET imaging of pancreatic cancer. *Clin. Cancer Res.* **22**, 3821–3830 (2016).
51. S. Zhu, R. Tian, A. L. Antaris, X. Chen, H. Dai, Near-infrared-II molecular dyes for cancer imaging and surgery. *Adv. Mater.* **31**, e1900321 (2019).
52. E. Fonsatti, H. J. M. Nicolay, M. Altomonte, A. Covre, M. Maio, Targeting cancer vasculature via endoglin/CD105: A novel antibody-based diagnostic and therapeutic strategy in solid tumours. *Cardiovasc. Res.* **86**, 12–19 (2010).
53. V. Q. Sier *et al.*, Endoglin/CD105-based imaging of cancer and cardiovascular diseases: A systematic review. *Int. J. Mol. Sci.* **22**, 4804 (2021).
54. K. Greish, *Cancer Nanotechnology* (Springer, 2010), pp. 25–37.
55. S. Gioux, H. S. Choi, J. V. Frangioni, Image-guided surgery using invisible near-infrared light: Fundamentals of clinical translation. *Mol. Imaging* **9**, 237–255 (2010).
56. C. Barth, S. Gibbs, Fluorescence image-guided surgery: A perspective on contrast agent development. *Proc. SPIE Int. Soc. Opt. Eng.* **11222**, 112220J (2020).
57. Q. Zhou *et al.*, EGFR-targeted intraoperative fluorescence imaging detects high-grade glioma with panitumumab-IRDye800 in a phase 1 clinical trial. *Theranostics* **11**, 7130-7143 (2021).

58. N. Nishio et al., Optimal dosing strategy for fluorescence-guided surgery with panitumumab-IRDye800CW in head and neck cancer. *Mol. Imaging Biol.* **22**, 156–164 (2020).

59. W. S. Tummers et al., Development and preclinical validation of a cysteine knottin peptide targeting integrin $\alpha v \beta 6$ for near-infrared fluorescent-guided surgery in pancreatic cancer. *Clin. Cancer Res.* **24**, 1667–1676 (2018).

60. Y. Sun et al., Novel bright-emission small-molecule NIR-II fluorophores for *in vivo* tumor imaging and image-guided surgery. *Chem. Sci. (Camb.)* **8**, 3489–3493 (2017).

61. X. Zeng et al., A bright NIR-II fluorescent probe for breast carcinoma imaging and image-guided surgery. *Chem. Commun. (Camb.)* **55**, 14287–14290 (2019).

62. LI-COR, IRDye 800CW protein labeling kit: High MW. https://www.licor.com/documents/xm4uuiso03nhbqqi2bdh51mu9godko15. Accessed 4 January 2000.

63. National Research Council, *Guide for the Care and Use of Laboratory Animals* (National Academies Press, Washington, DC, 2011), 8th Ed.